Applied Energy 269 (2020) 114948

Contents lists available at ScienceDirect

Applied Energy

journal homepage: www.elsevier.com/locate/apenergy

Subdermal solar energy harvesting – A new way to power autonomous electric implants

M.V. Tholl[a,c,g], H.G. Akarçay[b], H. Tanner[c], T. Niederhauser[f], A. Zurbuchen[g], M. Frenz[b,*], A. Haeberlin[a,c,d,e,g,*]

[a] ARTORG Center for Biomedical Engineering Research, Cardiovascular Engineering, University of Bern, Murtenstrasse 50, CH-3008 Bern, Switzerland
[b] Institute of Applied Physics, Biomedical Photonics, University of Bern, Sidlerstrasse 5, CH-3012 Bern, Switzerland
[c] Department of Cardiology, Inselspital, Bern University Hospital, University of Bern, Freiburgstrasse 4, CH-3010 Bern, Switzerland
[d] Electrophysiology and Heart Modeling Institute (LIRYC), Bordeaux University, Pessac, France
[e] Bordeaux University Hospital (CHU), Electrophysiology and Cardiac Stimulation Unit, F-33600 Pessac, France
[f] Institute for Human Centered Engineering, Bern University of Applied Sciences, Quellgasse 21, 2502 Biel, Switzerland
[g] sitem Center for Translational Medicine and Biomedical Entrepreneurship, University of Bern, Freiburgstrasse 3, 3010 Bern, Switzerland

HIGHLIGHTS

- Monte-Carlo simulations are used to calculate power of subdermal solar cells.
- Subcutaneous solar cells may replace batteries in implantable electronic devices.
- A cardiac pacemaker can be supplied by less than 10 min midday solar irradiation.
- Simulations revealed that the low wavelength range is strongly absorbed by skin.
- The subdermal fluence spectrum differs strongly from natural solar irradiance.
- Solar cell properties must be adapted for spectral subdermal fluence.

ARTICLE INFO

Keywords:
Cardiac pacing
Subdermal implant
Solar cell characteristics
Quantum dot solar cells
Implant power supply
Battery replacement

ABSTRACT

Subdermal solar harvesting has the potential to obviate the need for the periodic battery replacements as required in patients with cardiac pacemakers. The achievable power output of the subdermal solar module depends on implantation depth, optical skin properties and to an important part on solar cell characteristics. Monte Carlo simulations of light distribution in human skin were used to estimate the power output of subdermal solar cells under midday sunlight exposure in geographical mid-latitudes as a function of implantation depth and solar panel size. For the darkest skin type, the daily energy demand of a modern cardiac pacemaker (0.864 J at a power demand of 10 μW) can be provided by a 2 cm^2 solar cell implanted subdermally at a depth of 3 mm when exposed to just 11 min of midday, clear sky irradiance. Our study reveals that solar harvesting with relatively small solar cells if optimized for the spectral subdermal fluence has the potential to power cardiac pacemakers in all skin types within reasonable irradiation exposure times. Solar energy harvesting is very promising to power electronic implants.

1. Introduction

Active electronic implants are widely used to treat medical diseases. A prime example is the cardiac pacemaker (PM) for the treatment of bradyarrhythmias (diseases leading to an abnormal and slow heartbeat). PMs operate by activating the heart by electrical stimulation and are the most widely used active medical devices with more than one million implanted devices per year worldwide [1]. The power requirement of a modern single chamber PM is below 10 μW, which currently is supplied by primary batteries. An extensive study revealed that the batteries of PMs last on average for 7.2 years [2]. The median survival time for patients with a PM, however, was reported to be 8.5 years [3], which is longer than the average lifetime of the PM's battery. This discrepancy strongly contributes to the high PM replacement rate of approximately 25% according to a worldwide survey [1]. This number might even increase with the increasing life expectancy.

* Corresponding authors at: Freiburgstrasse 3, 3010 Bern, Switzerland (A. Haeberlin).
E-mail addresses: martin.frenz@iap.unibe.ch (M. Frenz), Andreas.Haeberlin@insel.ch (A. Haeberlin).

https://doi.org/10.1016/j.apenergy.2020.114948
Received 6 November 2019; Received in revised form 26 March 2020; Accepted 2 April 2020

Nomenclature

Acronyms

PM	cardiac pacemaker
MC	Monte Carlo
VF	volume fraction
UV	ultraviolet
λ	wavelength [nm]
μ_a	absorption coefficient [cm^{-1}]
μ_s'	reduced scattering coefficient [cm^{-1}]
g	anisotropy factor
n	index of refraction
ζ	fraction of light absorbed by the subdermal solar cell
scd	solar cell implantation depth [mm]
N_{abs}	number of absorbed photons in the solar cell
N_{tot}	number of launched photons
A_{sc}	top surface area of the solar cell [cm^2]
A_{surf}	top surface area of the model [cm^2]
$ASTMG173$	standard for global irradiance at midday under clear sky in geographical mid-latitudes
ϕ	photon flux [#photons $s^{-1}m^{-2}$]
EQE	External Quantum Efficiency
V_{OC}	open circuit voltage [V]
I_{SC}	short circuit current [A]
q	elementary charge [C]
FF	fill factor of a solar cell
P_{out}	power output of the subdermal solar cell [μW]
P_{req}	power required by a modern pacemaker [μW]
E_{out}	energy output of the subdermal solar cell [J]
E_{req}	energy requirement of a modern pacemaker for 24 h of cardiac pacing [J]
t_{exp}	exposure time of the solar cell to a certain illumination [min]
η	efficiency

Furthermore, the increasing treatment possibilities with electronic implants raise the need for intracorporeal energy harvesting.

Energy harvesting within the human body aims to improve the battery longevity of an electronic implant in order to lower the number of surgeries for battery replacements. This strategy allows for the minimum battery capacity to be reduced, and with it the overall volume of the device. Energy harvesters can use kinetic energy from low frequency movements [4,5] such as movements [6,7] or vibrations [8,9] of the heart. Other techniques harvest energy from blood pressure variations [10] or blood flow in the heart [11,12] or in large arteries [13]. Most biomedical energy harvesting mechanisms are based on electromagnetic induction, the triboelectric or piezoelectric effect. Romero et al. [14] analysed different potential implantation sites for kinetic energy harvesting and Tan et al. [15] presented a review on electromagnetic vibration harvesters. Each of the afore mentioned devices relies on moving parts or deformation, which leads to mechanical wear and potential replacement. Moreover, currrently implemented devices are mostly implanted deep within the body, requiring more invasive surgeries and implicating potential for severe complications at implantation sites such as the heart or large vessels. Thermal radiation could be used by thermoelectric generators. They are however limited to wearable applications due to the necessary temperature gradient across the device. A new approach to harvest thermal radiation from a human body uses special photovoltaic cells based on quantum dots that are able to absorb human heat radiation and convert it into electricity [16]. Subdermal solar cells offer a minimally invasive strategy for electrical energy generation within the body by utilizing the absorbed light, as illustrated in Fig. 1. They do not rely on moving parts or deformation, with the current state-of-the-art achieving a mean degradation rate of only 0.8% per year resulting in lifetimes of >25 years [17]. Initial work has shown that subdermal solar cells can power electronic implants in vitro under porcine skin [18,19], in mice [20], in pigs [21,22] and with wearable devices containing solar cells covered by optical filters mimicking Caucasian skin properties [23]. Based on such a wearable device in a human case study, Bereuter et al. [24] reported that the energy output of a 3.6 cm^2 subdermal solar cell is sufficient to drive a modern pacemaker. However, a detailed understanding is needed to identify the critical parameters affect the energy output of subdermal solar cells in different implantation scenarios. In this study, we will thoroughly evaluate the possibilities of subdermal solar harvesting for different skin types and implantation depths to provide the necessary information such as spectral range and skin transmittance needed for optimizing subdermal solar cells and for targeted planing of in vivo studies.

2. Methods

Monte Carlo (MC) methods were used to simulate the light fluence and the fraction of light absorbed in the solar cell at different subdermal depths. The MC simulations are based on optical skin properties such as the absorption coefficient μ_a [cm^{-1}], reduced scattering coefficient μ_s' [cm^{-1}], refractive index n and the anisotropy factor g. The goal is to provide a measure for calculating the maximum expected power output of any subdermal solar cell.

2.1. Optical properties of human skin

Human skin essentially consists of three main layers: a thin epidermal layer, the dermis, and the subdermis. The subdermis contains a variable amount of subcutaneous fat separating skin from muscle or bone. The skin's primary optical properties are the absorption coefficient μ_a, the reduced scattering coefficient μ_s', the index of refraction n, and the anisotropy factor g. Each of the three layers has distinct optical properties, and all are wavelength-dependent. Dermal optical properties have been described by various groups in literature [25–29]. The human skin can be divided into its components according to their volume fractions (VF). Table 1 summarizes the VFs used to calculate μ_a of the different skin layers. The epidermis is bloodless and has a varying melanosome VF for different skin types, whereas dermis and subcutaneous tissue do contain blood vessels. The 'Other VF' represents all the skin components not accounted for separately and was calculated by subtracting the sum of all known VFs from unity.

Human skin color can be classified into 6 different types [30].

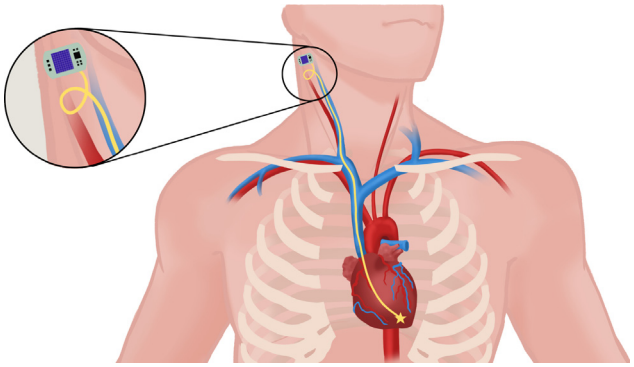

Fig. 1. Illustration of a solar cardiac pacemaker implanted subdermally in the neck. The pacing lead is inserted into the heart via the internal jugular and superior caval vein.

Table 1
Volume fractions (VF) of the skin's constituents within the three layers used as MC input. Melanosome is abbreviated by 'Melan.'.

Tissue	Blood VF	Water VF	Fat VF	Melan. VF	Other VF
Epidermis (type VI)	0 [35]	0.65 [35]	0.1 [35]	0.0165 [33]	0.2335 [36]
Dermis	0.02	0.75	0.2	0.01	0.02
Subcutaneous tissue	0.08	0.7	0.2	0.0095	0.105

Classification criteria include skin color, tanning characteristics and sensitivity to sunburning by UV radiation. Skin color ranges from a very light Type I (which is very likely to burn) to very dark Type VI (which usually does not burn). The melanosome VF of the epidermis for skin type VI are given in literature and represent the highest μ_a. However, the published VFs for the dermis and subcutaneous tissue result in estimated absorption coefficients that are lower than the ones experimentally determined [26–28,31]. Therefore, we adjusted the VFs of the skin constituents (in particular the melanosome VF) to obtain slightly higher absorption coefficients than all measured values found in literature. This assured we calculated the worst case scenario.

Brenner and Hearing [32] stated that the differences in skin color are not caused by a difference in the number of melanocytes but rather by their melanogenic activity. This results in larger size and number of melanosomes for darker skin types, which is reflected in melanosome volume fractions that are two [33] to five times [34] higher in dark skin (Type VI) compared to light skin (Type I). The darkest skin type (VI) was modelled with the according epidermal melanosome volume fractions given in literature.

2.1.1. Absorption coefficient μ_a

The absorption coefficient μ_a of a typical cutaneous melanosome was calculated according to Eq. (1) [29].

$$\mu_{a,melanosome}(\lambda) = 519\left(\frac{\lambda}{500}\right)^{-3} \quad (1)$$

The absorption coefficients of water [37], blood [38] and fat [39] are given in literature (see Fig. 2). Since μ_a values for fat are found only for the wavelength range between 434 nm and 1098 nm we extrapolated the values as being constant in the λ-ranges 400–434 nm and 1098–1200 nm.

The skin layer's individual absorption coefficients were calculated by summing up the contributions of each constituent's μ_a according to the respective VF within the layer (Table 1, Eq. (2)).

$$\mu_a = \sum VF_i\,\mu_{a,i} \quad (2)$$

Fig. 3 compares the calculated μ_a and literature values for epidermis (top), dermis (middle) and subcutaneous tissues (bottom). The calculated absorption values are plotted as red lines. Generally, all calculated μ_a values were slightly higher than the literature values. This yields to overestimated absorption within the skin to investigate the worst case scenario in terms of the fraction of light absorbed by the subdermal solar cell.

2.1.2. Reduced scattering coefficient μ_s'

The equation for the reduced scattering coefficient μ_s' of skin and subcutaneous tissue is given by Jacques [29]:

$$\mu_s' = a\left(\frac{\lambda}{500}\right)^{-b} \quad (3)$$

The coefficient a scales μ_s' and coefficient b - named the 'scattering power' - adjusts the λ-dependence of μ_s'. Both coefficients were adjusted to achieve a resulting μ_s' that is slightly higher than literature values for all wavelengths and skin layers, again to examine the worst case in our MC simulations. The final coefficients are summarized in Table 2.

Fig. 4 shows calculated reduced scattering coefficient μ_s' as red lines for the skin layers epidermis (top), dermis (middle) and subcutaneous tissues (bottom) compared to literature data [40].

2.1.3. Anisotropy and refractive indices

The anisotropy factor g was set to 0.9 for all tissues. The refractive indices were measured by Tearny et al. [41] as 1.34 for epidermis and 1.41 for dermis and subcutaneous fat.

2.2. Monte Carlo simulation

2.2.1. Monte Carlo method

An established and verified Monte Carlo code [42–44] was used to perform simulations using the calculated optical properties of human skin and a tissue model to simulate the light fluence and the fraction of light absorbed in the cell at different depths within the tissue model. The number of simulated photons was set to n = 10^7 based on a convergence study. The simulations were repeated for wavelengths between 400 nm and 1200 nm in 50 nm steps.

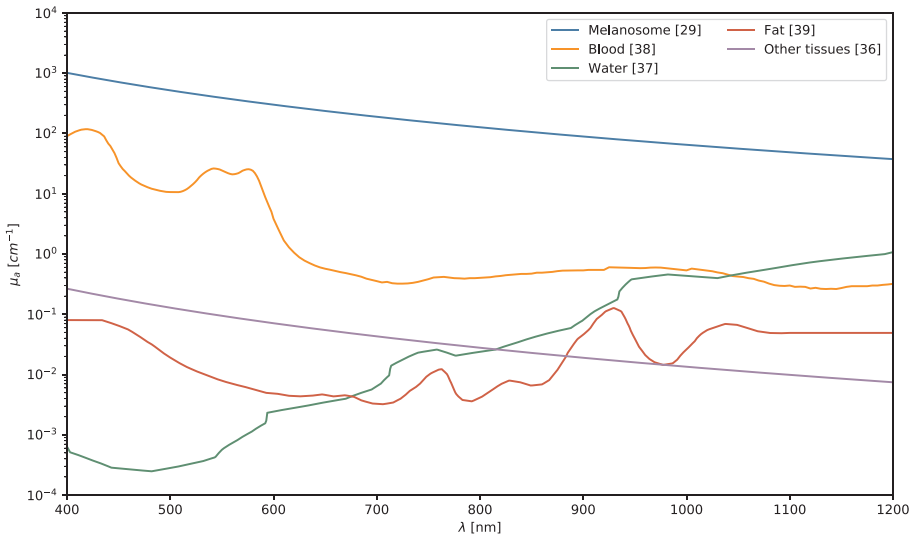

Fig. 2. Absorption coefficients $\mu_a(\lambda)$ [cm^{-1}] of the skin's constituents given in literature.

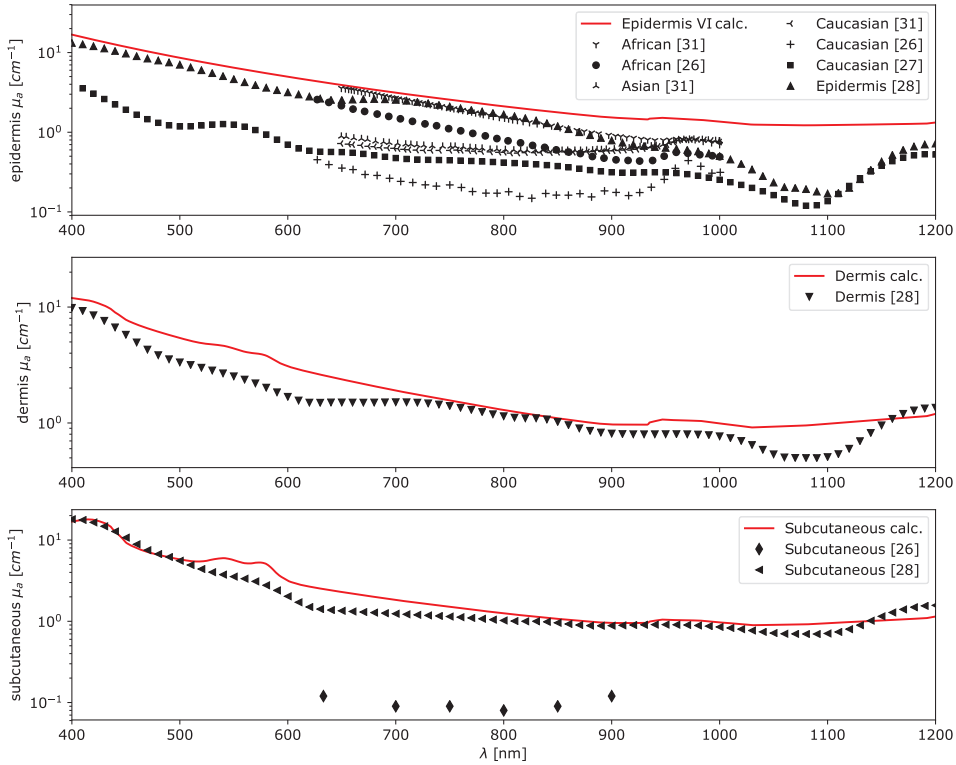

Fig. 3. Comparison of literature values and calculated absorption coefficients μ_a of human skin layers: epidermis (top), dermis (middle) and subcutaneous tissues (bottom).

Table 2
Coefficients a and b of Eq. (3), describing the skin layers' μ_s'.

Tissue	a	b
Epidermis (VI)	80	1.15
Dermis	60	1.4
Subcutaneous tissue	40	1

2.2.2. Tissue model geometry

The tissue model geometry is illustrated in Fig. 5. The model geometry was designed to minimize the fraction of photons escaping through the model boundaries. It consists of a cuboid shape with side lengths of 50 mm and a depth of 30 mm. Although skin is built up by a complex and heterogeneous structure in which the spatial concentration distribution of absorbing chromophores and blood is strongly depth dependent, it can be approximated by a multi-layered medium with layers characterized by constant optical properties [36,45]. This was realized by discretizing the model with 1000*1000*600 voxels and vertically dividing it into 4 layers: air, epidermis, dermis, and subcutaneous tissue. The air layer allowed to calculate the reflection of the incoming light at the air/epidermis interface. The irradiance was assumed to be normal and homogenous across the skin surface. The epidermis layer was 0.1 mm thick. The dermis layer had a thickness of 1.4 mm, which is a conservative assumption of the thickness in the anterior neck region, an intended site for device implantation [46,47]. The subcutaneous tissue layer filled the remaining model, except for a highly absorbing (μ_a = 10'000 cm^{-1}), index matched solar cell in the center of the model with side lengths of $\sqrt{2}$ cm and a thickness of 0.5 mm. During MC simulations, the solar cell's implantation depths scd [mm] was varied between 1.5 mm and 4.5 mm.

2.2.3. Fraction of light absorbed by the solar cell

The outcome of interest is the fraction of light absorbed by the solar cell (ζ) as a function of wavelength and implantation depth. ζ was calculated according to Eq. (4).

$$\zeta(\lambda, scd) = \frac{N_{abs}/A_{sc}}{N_{tot}/A_{surf}} \tag{4}$$

N_{abs} is the number of absorbed photons within the solar cell volume and N_{tot} is the total number of photons launched. A_{sc} and A_{surf} are the top surface areas of the solar cell and the model surface respectively.

2.3. Expected power output calculation

The expected clear sky, spectral irradiance for geographical mid latitudes and midday at sea level was defined by the global standard spectrum *ASTMG*173 [48]. *ASTMG*173 describes the global irradiance on a surface that is tilted by 37° from the horizon at air mass 1.5. The total irradiance of *ASTMG*173 is 1000 Wm^{-2}. The subdermal irradiance absorbed by the cell can be calculated by multiplying the spectral irradiance with $\zeta(\lambda, scd)$. The photon flux ϕ [#photons $s^{-1}m^{-2}$] can be calculated by dividing the irradiance by the photon energy at the respective wavelength.

Each solar cell has its own individual External Quantum Efficiency (*EQE*). This characteristic describes the number of electrons collected at the cell's contacts per incident photon. It is λ-dependent and reveals the spectrum where the solar cell exhibits optimum performance (approx. 400–1000 nm for monocrystalline silicon solar cells). Moreover, each solar cell is characterized by an irradiance dependent open circuit voltage V_{OC}. The combination of *EQE* and the V_{OC} determines the theoretical power output of the solar cell. The solar cell's short circuit current I_{SC} [Am^{-2}] at depth *scd* is calculated according to Eq. (5), where q [C] is the elementary charge.

$$I_{SC}(\lambda, scd) = \int_{\lambda=400\ nm}^{1200\ nm} \phi(\lambda)\,\zeta(\lambda, scd)\,EQE(\lambda)\,q\,d\lambda \tag{5}$$

The open circuit voltage V_{OC} [V] is also determined by the subdermal irradiance. Usually, solar cells are connected to an electronic circuit that maximizes the power ouput P_{out} [W] of the solar cells. One common

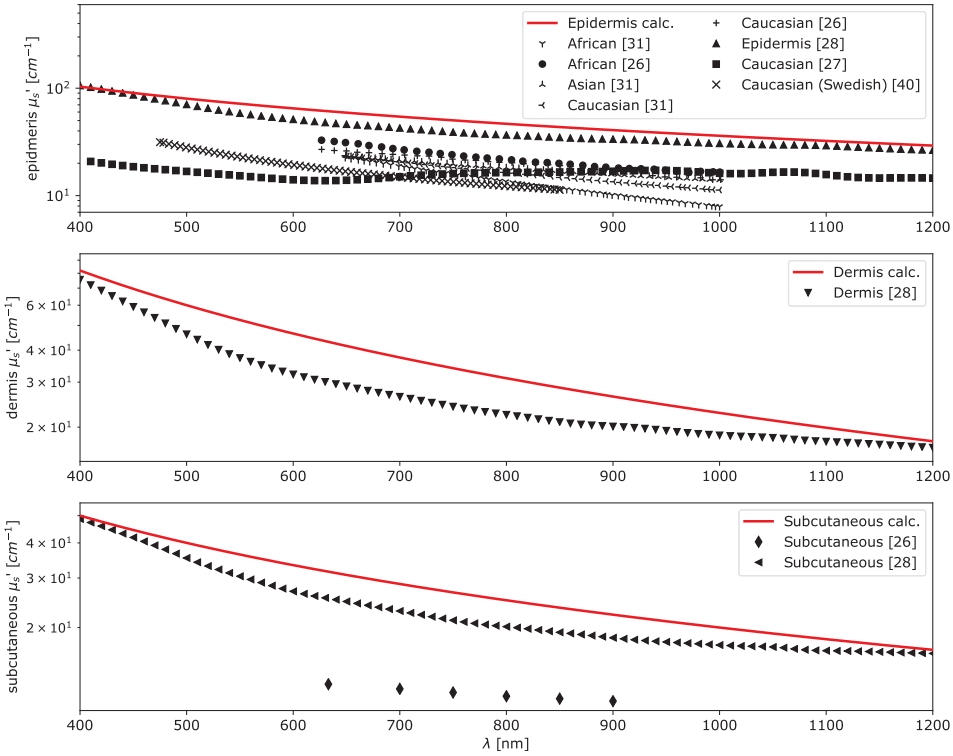

Fig. 4. Comparison of literature values and calculated reduced scattering coefficients μ_s' of human skin layers: epidermis (top), dermis (middle) and subcutaneous tissues (bottom).

practice is to connect maximum power point trackers to solar cells which adjust their input impedance to reach the optimal efficiency of the cell. P_{out} of the solar cell with area A_{SC} [m^2] is defined by Eq. (6). The fill factor *FF* is a characteristic of solar cells associated to the maximum power output. For highly-efficient monocrystalline silicon cells FF is typically around 0.8 [49].

$$P_{out} = FF\ V_{OC}\ I_{SC}\ A_{SC} \tag{6}$$

Modern cardiac pacemakers have an average power requirement P_{req} of approximately 10 μW. The required energy E_{req} to operate a PM for an exemplary time of 24 h results to be 0.24 mWh or 0.864 J.

3. Results

MC simulations were used to calculate the light fluence and the fraction of light absorbed in the solar cell for different wavelengths and depths within the tissue model. Fig. 6 shows the light fluence normalized to the maximum value of each wavelengths along the central z-axis of the model for skin type VI without a solar cell. At a depth of 6 mm, almost all light is absorbed. The light penetration depth strongly decreases for shorter wavelengths, especially for $\lambda < 900$ nm. The fact that the fluence just below the surface is larger than the irradiance at the surface is due to backscattering and the small value of μ_a with respect to μ_s'.

3.1. Fraction of light absorbed in the cell at different depths

Fig. 7 shows the simulated fraction of light absorbed in the solar cell (ζ) at different wavelengths and solar cell implantation depths for the darkest skin (type VI). Generally, ζ decreases towards shorter wavelengths. The fraction of light absorbed in the cell is close to zero at $\lambda <$ 550 nm, especially for deeper implantation depths. Overall, ζ decreases

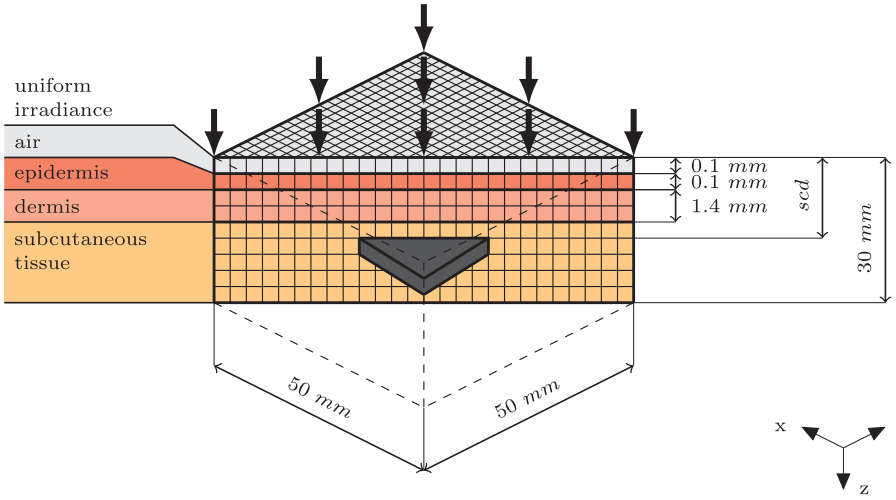

Fig. 5. Partial cross-sectional view of the skin model geometry. The whole model is cut along the diagonal except for the central solar cell (black) placed at varying implantation depths *scd*. The 4 different layers are colored (air, epidermis, dermis and subcutaneous tissue from top to bottom). The uniform irradiance (number of photons: n = 10^7) strikes the entire surface of the model and is illustrated by black arrows. The dashed lines show the outline of the cut geometry. The grid and the layer thicknesses are not a true to scale representation.

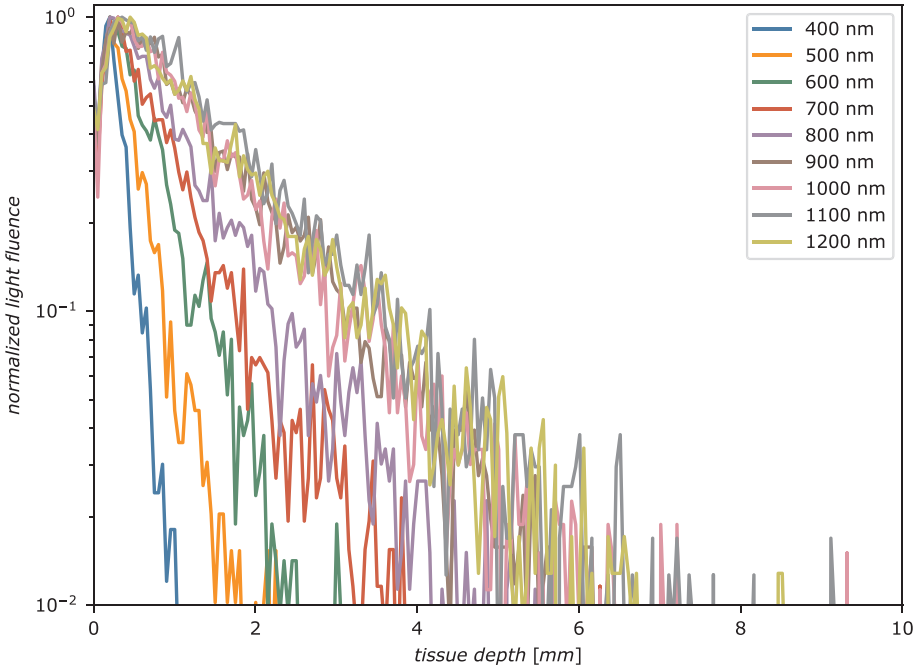

Fig. 6. Exponential decrease of the normalized light fluence along the central z-axis of the model for skin type VI without a solar cell.

logarithmically with *scd* along the same wavelength.

The fraction of the total solar power absorbed by the cell at different implantation depths is summarized in Table 3. It is calculated by integrating reference and subdermal irradiance on the solar cell at different depths over wavelength and dividing the subdermal power by the reference power. At a realistic implantation depth of 3 mm, the overall power of the irradiance is reduced to 3.51% of the initial reference irradiance for our skin model with conservative assumptions for absorption and scattering values.

Table 3
Fraction of absorbed solar power by a subdermal (human skin type VI) cell at different implantation depth for wavelengths 400–1200 nm.

Skin tissue depth [mm]	Fraction of absorbed solar power [%]
1.5	13.66
2	8.64
2.5	5.47
3	3.51
3.5	2.27
4	1.50
4.5	0.97

3.2. Energy output of subdermal solar cells

The simulated fraction of light absorbed by the solar cell (ζ) is used to calculate the expected power output of the subdermal solar cell P_{out}. Fig. 8 shows the standard sea level global solar irradiance for solar system testing (ASTMG173, black) and the subdermal solar irradiance at an implantation depth of 3 mm (green). The skin's ζ at an implantation depth of 3 mm is shown in blue and the *EQE* of a high-

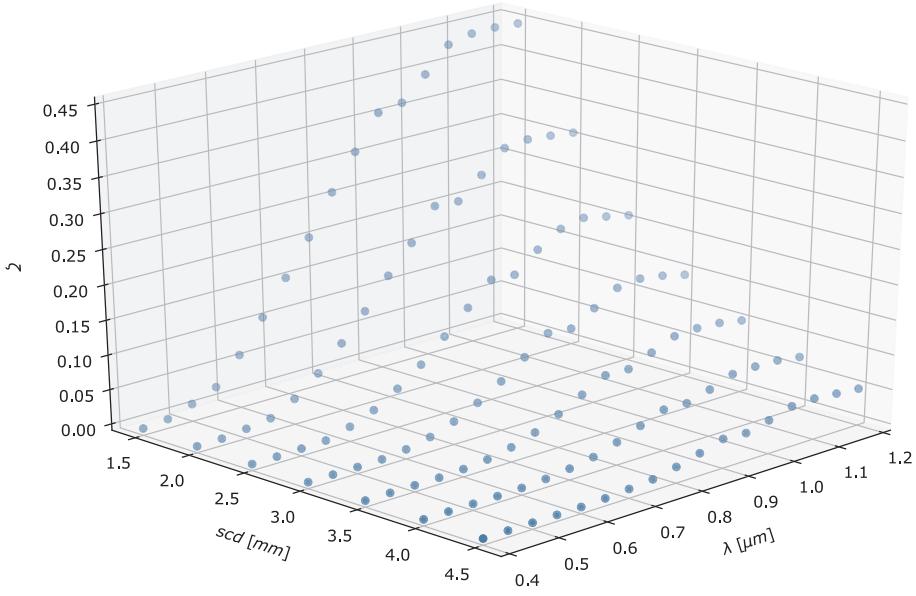

Fig. 7. 3D-plot of the skin type VI's fraction of light absorbed in the cell (ζ) in dependence of wavelength (λ) and the solar cell implantation depth (*scd*).

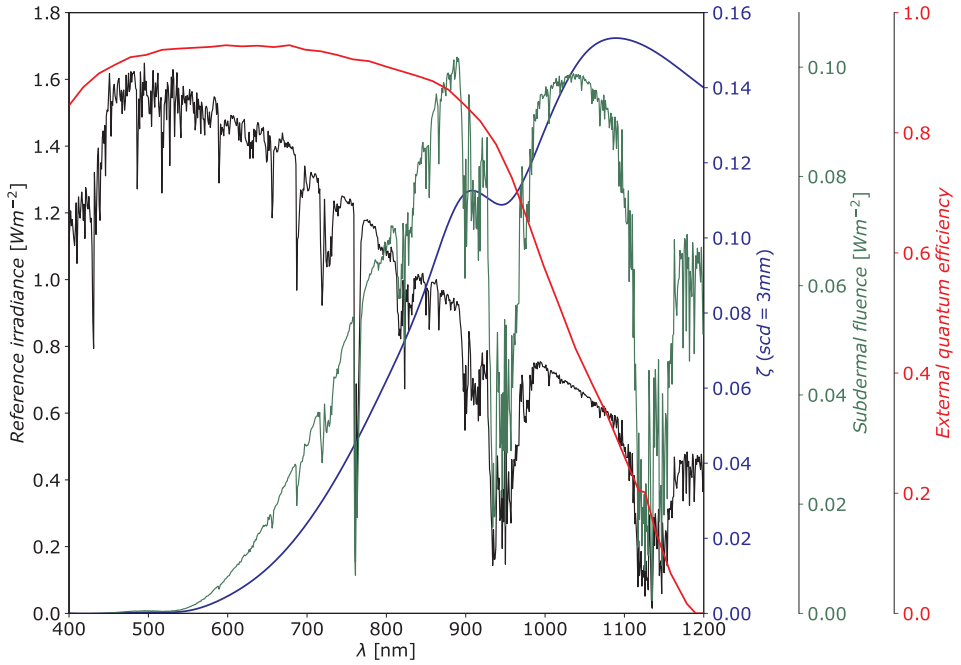

Fig. 8. The standard sea level global solar irradiance for solar system testing ASTMG173 is shown in black. The fraction of light absorbed by the solar cell (ζ, blue) results in a subdermal fluence absorbed by the cell at an implantation depth (*scd*) of 3 mm (green). An exemplary external quantum efficiency EQE (red) shows the characteristic of a monocrystalline silicon solar cell. All plots share the same x-axis but have their individual y-axis with ticks in the same color as the graph.

performance monocrystalline silicon solar cell (IXOLAR^{TM}, IXYS Corporation, Milpitas, California, USA) with a rated efficiency η of 22% is plotted in red. The perfect overlap of the solar irradiance intensity and the EQE reveals that monocrystalline silicon solar cells are well optimized for direct illumination. However, the subdermal fluence shows a different spectral distribution of which strongly increases for wavelengths above 550 nm. The light at $\lambda < 550$ nm is absorbed in the first 3 mm of skin tissue. The subdermal fluence is highest when the EQE of the monocrystalline solar cell starts to decrease.

The expected power output P_{out} is calculated according to Eqs. (5) and (6), assuming a solar cell area of 2 cm^2. P_{out} is evaluated at different implantation depths *scd* and for varying exposure times t_{exp}, resulting in an energy output E_{out} (illustrated in Fig. 9). E_{out} is linearly increasing with increasing t_{exp} within one implantation depth. The slope of the $E_{out}(t_{exp})$ is decreasing for increasing implantation depth, resulting in less energy output at deeper implantation sites. The red line in Fig. 9 connects the points for which the energy requirement (E_{req} = 0.864 J) to run a cardiac pacemaker for 24 h without illumination is met. This line has been projected to the base xy-plane to improve readability of the required t_{exp}. The red projected, dashed line shows the minimum irradiation time necessary to provide enough energy to power a modern PM for 24 h. The calculation assumes a solar cell area of 2 cm^2, midday, clear sky irradiation in western latitudes and 100% efficiency in energy storage. At an implantation depth of 3 mm (within the subcutaneous tissue), the required t_{exp} results in 11 min. At the deepest evaluated implantation depth of 4.5 mm, the required t_{exp} increases to 45.5 min.

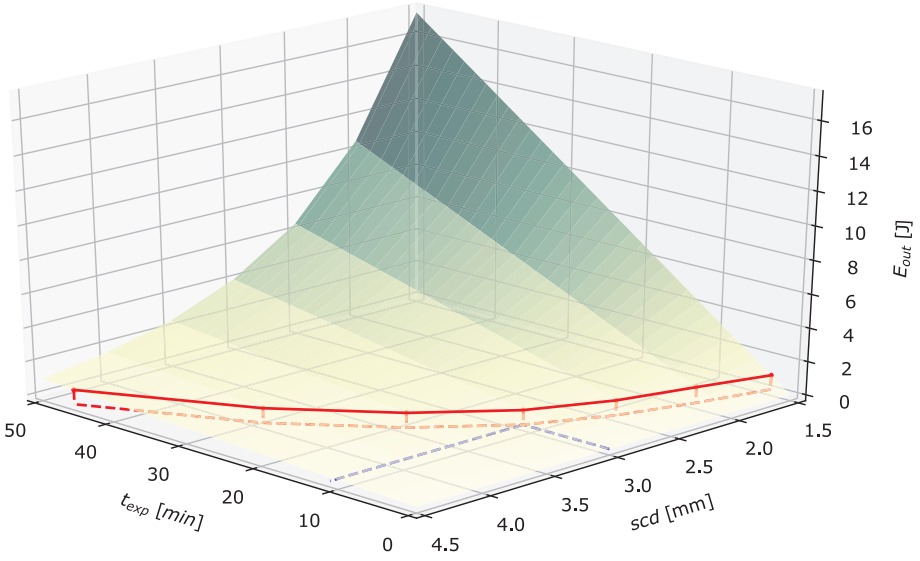

Fig. 9. 3D-plot of the expected energy output of the solar cell in dependence of exposure time (t_{exp}) and the solar cell implantation depth (*scd*) under skin type VI. The red horizontal line connects the points where the minimum energy requirement is met for running a modern, single-chamber pacemaker during 24 h. It is projected to the base xy-plane (red dashed line). The blue dashed lines indicate an exemplary readout of the necessary t_{exp} at *scd* = 3 mm.

4. Discussion

The goal of our study was to determine under which conditions subdermal solar harvesting is feasible and to elaborate on its limitations. In all cases, we performed all our calculations based on a worst case scenario in terms of the fraction of light absorbed by the subdermal solar cell. This was done using optical absorption and scattering values that are slightly higher than published experimentally determined values for our MC simulations and assuming the darkest skin type VI (see Fig. 3 and 4). In addition, we assumed a full skin thickness of 1.5 mm, which is also slightly thicker than published values [46,47].

4.1. Solar cell

Enlarging the area of the solar cell increases the power production for a given irradiance. For a subdermal application however, this contradicts patient comfort and leads to a more invasive implantation. Moreover, since the cell will be visible through the skin, its area should be minimized to comply with the aesthetic interest of the patients. Therefore, the energy output was evaluated for a solar cell with an active area of 2 cm^2, which is significantly smaller than the footprint of a modern cardiac pacemaker and is a compromise between sufficient power output on one side and acceptable invasiveness and aesthetics on the other side.

The power output was evaluated for a highly efficient monocrystalline silicon solar cell, which is well optimized for direct irradiance with its maximum EQE around 500–700 nm (compare Fig. 8). The subdermal fluence however shows the highest values at λ from 800 nm to 1100 nm. A solar cell with an EQE comparable to monocrystalline silicon solar cells but an optical sensitivity expanding into the near IR-range (around 1200 nm) would strongly increase the harvested energy, allowing either a reduction in cell area or a decrease in illumination time. This could be achieved by using solar cells with multiple pn-junctions of different semiconductor materials. These materials absorb photons at distinct λ-bands and are generally more efficient than monocrystalline silicon solar cells. The individual layers of a multi-junction cell are usually connected in series [50]. Therefore, the layer with the lowest current limits the overall current of the stacked cell. The measured efficiencies of these multi-junction cells refer to solar irradiation on earth. However, they will change if the subdermal fluence is considered. Because of the skin's high absorption in the near-UV range, one layer of the multi-junction cell might generate a very low current, which in turn limits the other layers of the cell. This can drastically reduce the power output of a multi-junction solar cell within the body. Peraca et al. [51] analyzed the EQE frequency response of a GaInP/GaAs/GaInNAs multi-junction solar cell. They showed that the EQE response is high for GaInP at 400–600 nm, for GaAs at 650–900 nm and for GaInNAs at 900–1200 nm. Therefore, a double junction solar cell with GaAs and GaInNAs layers can reach a higher efficiency than monocrystalline solar cells under subdermal irradiation. A solar cell with GaAs and GaInNAs layers would reduce t_{exp} by 27% (8 min instead of 11 min) compared to a standard monocrystalline silicon cell.

Recent studies have shown that quantum dots photovoltaic cells can be tuned to match the spectral distribution of solar or any irradiation spectrum. This is done by changing size, shape and composition of the quantum dots. In addition, quantum dot based solar cells have the potential to boost solar power efficiency from about 20% (standard crystalline solar cells) to about 66% [52]. For example, Ghomian et al. [16] presented a new approach to biomedical energy harvesting by pushing the spectral sensitivity into the mid-IR range (1–14 μm) using a lead sulfide colloidal quantum dot photovoltaic cell. Quantum dot cells have the potential to harvest energy from human body thermal radiation to drive low power devices such as cardiac pacemakers. Assuming an optimized solar cell having a constant external quantum efficiency of 95% over the whole spectral range from 400 nm to 1200 nm, which could be realized by a quantum dot photovoltaic cell, would further reduce t_{exp} by 10% to an irradiation time of only seven minutes.

4.2. Light propagation through skin tissue

Previous work [22] obtained a median power output of 1963 μW/cm^2 from a 4.6 cm^2 monocrystalline silicon solar cell covered by an explanted pig skin flap with a thickness of 4.8 mm. The irradiance on the skin was 842 W/m^2 under global solar irradiation, which means that 2.33% of the initial irradiance was converted to electrical energy. The diffuse solar irradiance in the shade was 120 W/m^2 and resulted in a power output of the solar cell of 206 μW/cm^2. This corresponds to a total fraction of light absorbed in the cell and power conversion of 1.72%. Indoors irradiance was measured at 4 W/m^2 and resulted in a power output of 4 μW/cm^2 for the subdermal solar cell. Therefore, the total fraction of light absorbed in the cell and conversion of indoors irradiance was about 1%.

The differences in fraction of light absorbed in the cell and power conversion depending on the type of irradiance can be explained by the different spectral distributions of direct sunlight, shade (diffuse light) and indoors irradiance. The fraction of light absorbed by the solar cell as simulated in this study was only 0.97% for outdoor irradiation at an implantation depth of 4.5 mm. Assuming an efficiency of 0.2 for an exemplary solar cell, the expected power conversion of the subdermal solar cell is 0.19%, which is more than an order of magnitude lower than the experimental results published by Haeberlin et al. [22].

The big difference in the results can be explained by the fact that pig skin, although it is considered as the most accurate skin animal model compared to humans in terms of physiology, cellular composition and anatomy [53], differs strongly from the human skin simulated in this study in terms of optical properties, having a much lower pigmentation. Moreover, the abovementioned pig skin was explanted post-mortem and bloodless. Our simulations were based on a worst case scenario assuming a very high pigmentation corresponding to skin type VI. In addition, we overestimated the skin's scattering characteristics, leading to smaller fractions of absorbed light in the solar cell.

Adjusting the optical properties to the measured Caucasian skin values increases the fraction of light absorbed by the solar cell significantly and leads to a reduction of necessary t_{exp} to less than 5 min compared to the 11 min in our worst case scenario.

4.3. Energy storage

The energy output of the subdermal cell would be stored in e.g. a rechargeable battery with sufficient capacity to overcome periods of darkness or lower irradiance. The energy storage's capacity could be reduced from about 7 years (primary batteries) to about 1 year (rechargeable battery), which is the usual check-up period for pacemaker patients. The capacity could be reduced even further considering the option of charging using artificial light. The energy storage solution should tolerate short and high cycles of loading and unloading.

4.4. Implantation site

Ideally, the subdermal solar cell will be implanted at a sun-exposed and hairless site as for example the neck. The implantation requires a surgery - causing scar formation and encapsulation of the solar cell. The scar tissue and encapsulation consist mainly of collagen [54]. Since collagen has lower absorption and reduced scattering coefficients than the dermis [55], scar formation and encapsulation was not considered in our simulations. First animal trials *in-* and *ex-vivo* generated reference data, however the differences in physiology and - in the case of *ex-vivo* measurements - perfusion are not negligible. Future *in vivo* human trials are necessary to study the effects of wound healing and of perfusion and to validate our simulations.

4.5. Artificial illumination

All our simulations assumed sea level global solar irradiance measured at clear sky conditions at midday for geographical mid latitudes. Depending on the weather conditions, season, and time of day, the irradiance might be considerably lower and spectrally shifted. Moreover, the location and altitude changes the irradiance as well, especially at different latitudes. Increasing altitude decreases the pathlength of light through the atmosphere and therefore increases irradiance. Haeberlin et al. [22] measured that the diffuse irradiance in the shade is reduced by a factor of 7 when compared to direct clear sky irradiance at a sun elevation of 65°. Indoor office irradiance was measured to be 210 times lower.

Indoor lighting can generate significant power [24]. Artificial light sources in buildings have emission spectra that vary with the technology used to emit light. LED lights usually provide narrow spectral irradiance bands between 400 and 700 nm depending on their color. Halogen lamps emit a broad spectral irradiance from 400 to > 1100 nm and are therefore more beneficial for the power output of a subdermal solar cell [56].

Our presented method aims towards autonomous implants that will be charged using the daily available natural and indoor light. However, an optimized artificial light source could also be used to efficiently charge the implant. This optimized light source (near-IR) could reach deeper implantation depths than natural light, without burning the skin. The possibility to charge the implant in greater depths would solve the problem of the cell's visibility. Charging through artificial light could also be considered as a backup solution for people with very low light exposure. A halogen lamp (250 W) in 0.5 m distance to the implanted solar cell produces an irradiance with less than 10% of the midday's solar power in the wavelength range between 400 and 1200 nm. Such artificial illumination would generate sufficient energy to run a solar pacemaker for 24 h operation in darkness within 150 min, which could however drastically be reduced using a light source emitting light in a spectral region perfectly adapted to the skin's transmission and to the wavelength sensitivity of the implanted solar cell.

5. Conclusion

We present an adjustable model to estimate the power output of a subdermal solar energy harvester for electronic implants. Subdermal energy harvesting can be used for many different applications and is not restricted to cardiac pacing. Other applications may include implanted sensors to more accurately measure blood pressure, or acceleration sensors to detect falls or accidents for the elderly. The presented Monte Carlo methodology allows to estimate a subdermal solar cell's energy output for different exposure times, implantation depths, skin types and cell sizes, making it applicable for implants with different power demands. Our simulation revealed the need for developing special solar cells optimized for near-infrared radiation in order to minimize the irradiation time requested for an efficient applicability of subdermal solar harvesting for medical power devices for all skin types. Our study shows promising results and suggests applicability of subdermal solar harvesting for medical low power devices for all skin types. The subdermal solar harvester could increase the lifetime of the implant, which, in turn, reduces the number of required implant replacements and the overall implant volume, increasing the comfort of the patient.

6. Data availability

All data used in this study is available upon request to the corresponding author.

Credit authorship contribution statement

M.V. Tholl: Conceptualization, Methodology, Investigation, Validation, Software, Visualization, Writing - original draft. **H.G. Akarçay:** Methodology, Conceptualization, Validation, Software, Writing - review & editing. **H. Tanner:** Funding acquisition, Writing - review & editing, Supervision. **T. Niederhauser:** Supervision, Writing - review & editing. **A. Zurbuchen:** Supervision, Writing - review & editing. **M. Frenz:** Supervision, Methodology, Conceptualization, Writing - review & editing. **A. Haeberlin:** Funding acquisition, Writing - review & editing, Supervision, Project administration.

Declaration of Competing Interest

The authors declare that they have no known competing financial interests or personal relationships that could have appeared to influence the work reported in this paper.

Acknowledgments

This research was supported by the Velux Foundation (Project number 1051). The authors thank Joe Tesar for his contribution and Act-Inno AG for the access to their testing facilities. Declarations of interest: None.

References

[1] Mond HG, Proclemer A. The 11th world survey of cardiac pacing and implantable cardioverter-defibrillators: Calendar year 2009-a world society of arrhythmia's project. Pacing Clin Electrophysiol 2011;34(8):1013–27. https://doi.org/10.1111/j.1540-8159.2011.03150.x.

[2] Katz D, Akiyama T. Pacemaker longevity: The world's longest-lasting VVI pacemaker. Ann Noninvasive Electrocardiol 2007;12(3):223–6. https://doi.org/10.1111/j.1542-474x.2007.00165.x.

[3] Brunner M. Long-term survival after pacemaker implantation prognostic importance of gender and baseline patient characteristics. Eur Heart J 2004;25(1):88–95. https://doi.org/10.1016/j.ehj.2003.10.022.

[4] Janphuang P, Lockhart RA, Isarakorn D, Henein S, Briand D, de Rooij NF. Harvesting energy from a rotating gear using an AFM-like MEMS piezoelectric frequency up-converting energy harvester. J Microelectromech Syst 2015;24(3):742–54. https://doi.org/10.1109/jmems.2014.2349794.

[5] Pillatsch P, Yeatman EM, Holmes AS. A piezoelectric frequency up-converting energy harvester with rotating proof mass for human body applications. Sensors Actuators A: Phys 2014;206:178–85. https://doi.org/10.1016/j.sna.2013.10.003.

[6] Zurbuchen A, Pfenniger A, Stahel A, Stoeck CT, Vandenberghe S, Koch VM, et al. Energy harvesting from the beating heart by a mass imbalance oscillation generator. Ann Biomed Eng 2012;41(1):131–41. https://doi.org/10.1007/s10439-012-0623-3.

[7] Zurbuchen A, Haeberlin A, Bereuter L, Pfenniger A, Bosshard S, Kernen M, et al. Endocardial energy harvesting by electromagnetic induction. IEEE Trans Biomed Eng 2017:1. https://doi.org/10.1109/tbme.2017.2773568.

[8] Ansari M, Karami MA. A sub-cc nonlinear piezoelectric energy harvester for powering leadless pacemakers. J Intell Mater Syst Struct 2017. https://doi.org/10.1177/1045389x17708344. 1045389X1770834.

[9] Ansari MH, Karami MA. Experimental investigation of fan-folded piezoelectric energy harvesters for powering pacemakers. Smart Mater Struct 2017;26(6):065001https://doi.org/10.1088/1361-665x/aa6cfd.

[10] Deterre M, Lefeuvre E, Zhu Y, Woytasik M, Boutaud B, Molin RD. Micro blood pressure energy harvester for intracardiac pacemaker. J Microelectromech Syst 2014;23(3):651–60. https://doi.org/10.1109/jmems.2013.2282623.

[11] Haeberlin A, Rosch Y, Tholl MV, Gugler Y, Okle J, Heinisch PP, et al. Intracardiac turbines suitable for catheter-based implantation - an approach to power battery- and leadless cardiac pacemakers? IEEE Trans Biomed Eng 2020;67(4):1159–66. https://doi.org/10.1109/tbme.2019.2932028.

[12] Tholl MV, Haeberlin A, Meier B, Shaheen S, Bereuter L, Becsek B, et al. An intracardiac flow based electromagnetic energy harvesting mechanism for cardiac pacing. IEEE Trans Biomed Eng 2019;66(2):530–8. https://doi.org/10.1109/tbme.2018.2849868.

[13] Wang D-A, Chiu C-Y, Pham H-T. Electromagnetic energy harvesting from vibrations induced by kármán vortex street. Mechatronics 2012;22(6):746–56. https://doi.org/10.1016/j.mechatronics.2012.03.005.

[14] Romero E, Warrington R, Neuman M. Body motion for powering biomedical devices. In: 2009 Annual International Conference of the IEEE Engineering in Medicine and Biology Society, IEEE, 2009. https://doi.org/10.1109/iembs.2009.5333329.

[15] Tan Y, Dong Y, Wang X. Review of MEMS electromagnetic vibration energy harvester. J Microelectromech Syst 2017;26(1):1–16. https://doi.org/10.1109/jmems.2016.2611677.

[16] Ghomian T, Kizilkaya O, Choi J-W. Lead sulfide colloidal quantum dot photovoltaic cell for energy harvesting from human body thermal radiation. Appl Energy 2018;230:761–8. https://doi.org/10.1016/j.apenergy.2018.09.004.

[17] Jordan DC, Kurtz SR. Photovoltaic degradation rates - an analytical review. Prog

Photovoltaics Res Appl 2011;21(1):12–29. https://doi.org/10.1002/pip.1182.
[18] Wu T, Redoute J-M, Yuce MR. A wireless implantable sensor design with subcutaneous energy harvesting for long-term IoT healthcare applications. IEEE Access 2018:35801–8. https://doi.org/10.1109/access.2018.2851940.
[19] Chen Z, Law M-K, Mak P-I, Martins RP. A single-chip solar energy harvesting IC using integrated photodiodes for biomedical implant applications. IEEE Trans Biomed Circ Syst 2017;11(1):44–53. https://doi.org/10.1109/tbcas.2016.2553152.
[20] Song K, Han JH, Lim T, Kim N, Shin S, Kim J, et al. Subdermal flexible solar cell arrays for powering medical electronic implants. Adv Healthcare Mater 2016;5(13):1572–80. https://doi.org/10.1002/adhm.201600222.
[21] Haeberlin A, Zurbuchen A, Schaerer J, Wagner J, Walpen S, Huber C, et al. Successful pacing using a batteryless sunlight-powered pacemaker. Europace 2014;16(10):1534–9. https://doi.org/10.1093/europace/euu127.
[22] Haeberlin A, Zurbuchen A, Walpen S, Schaerer J, Niederhauser T, Huber C, et al. The first batteryless, solar-powered cardiac pacemaker. Heart Rhythm 2015;12(6):1317–23. https://doi.org/10.1016/j.hrthm.2015.02.032.
[23] Burks S, Kolcun JP, Wang MY. Subcutaneous solar cells harvest energy for pulse generation. Neurosurgery 2017;81(3):N24. https://doi.org/10.1093/neuros/nyx371.
[24] Bereuter L, Williner S, Pianezzi F, Bissig B, Buecheler S, Burger J, et al. Energy harvesting by subcutaneous solar cells: A long-term study on achievable energy output. Ann Biomed Eng 2017;45(5):1172–80. https://doi.org/10.1007/s10439-016-1774-4.
[25] Chan E, Sorg B, Protsenko D, O'Neil M, Motamedi M, Welch A. Effects of compression on soft tissue optical properties. IEEE J Sel Top Quantum Electron 1996;2(4):943–50. https://doi.org/10.1109/2944.577320.
[26] Simpson CR, Kohl M, Essenpreis M, Cope M. Near-infrared optical properties of ex-vivo human skin and subcutaneous tissues measured using the monte carlo inversion technique. Phys Med Biol 1998;43(9):2465–78. https://doi.org/10.1088/0031-9155/43/9/003.
[27] Bashkatov AN, Genina EA, Kochubey VI, Tuchin VV. Optical properties of human skin, subcutaneous and mucous tissues in the wavelength range from 400 to 2000nm. J Phys D: Appl Phys 2005;38(15):2543–55. https://doi.org/10.1088/0022-3727/38/15/004.
[28] Salomatina E, Jiang B, Novak J, Yaroslavsky AN. Optical properties of normal and cancerous human skin in the visible and near-infrared spectral range. J Biomed Opt 2006;11(6):064026https://doi.org/10.1117/1.2398928.
[29] Jacques SL. Optical properties of biological tissues: a review. Phys Med Biol 2013;58(11):R37–61. https://doi.org/10.1088/0031-9155/58/11/r37.
[30] Fitzpatrick TB. The validity and practicality of sun-reactive skin types i through VI. Arch Dermatol 1988;124(6):869. https://doi.org/10.1001/archderm.1988.01670060015008.
[31] Tseng S-H, Grant A, Durkin AJ. In vivo determination of skin near-infrared optical properties using diffuse optical spectroscopy. J Biomed Opt 2008;13(1):014016https://doi.org/10.1117/1.2829772.
[32] Brenner M, Hearing VJ. The protective role of melanin against UV damage in human skin†. Photochem Photobiol 2007;84(3):539–49. https://doi.org/10.1111/j.1751-1097.2007.00226.x.
[33] Te-Yu T, Chun-Yu C, Yi-Shan L, Kung-Bin S. Quantification of the optical properties of two-layered turbid media by simultaneously analyzing the spectral and spatial information of steady-state diffuse reflectance spectroscopy. Biomed Opt Exp 2011.
[34] Karsten AE, Smit JE. Modeling and verification of melanin concentration on human skin type. Photochem Photobiol 2011;88(2):469–74. https://doi.org/10.1111/j.1751-1097.2011.01044.x.
[35] Jacques SL. Optical assessment of cutaneous blood volume depends on the vessel size distribution: a computer simulation study. J Biophotonics 2009;3(1–2):75–81. https://doi.org/10.1002/jbio.200900085.
[36] Meglinski IV, Matcher SJ. Quantitative assessment of skin layers absorption and skin reflectance spectra simulation in the visible and near-infrared spectral regions. Physiol Meas 2002;23(4):741–53. https://doi.org/10.1088/0967-3334/23/4/312.
[37] Yoon G, Welch A, Motamedi M, Gemert M. Development and application of three-dimensional light distribution model for laser irradiated tissue. IEEE J Quantum Electron 1987;23(10):1721–33. https://doi.org/10.1109/jqe.1987.1073224.
[38] Bosschaart N, Edelman GJ, Aalders MCG, van Leeuwen TG, Faber DJ. A literature review and novel theoretical approach on the optical properties of whole blood. Lasers Med Sci 2013;29(2):453–79. https://doi.org/10.1007/s10103-013-1446-7.
[39] van Veen RL, Sterenborg H, Pifferi A, Torricelli A, Cubeddu R. Determination of VIS- NIR absorption coefficients of mammalian fat, with time- and spatially resolved diffuse reflectance and transmission spectroscopy. Biomedical topical meeting OSA; 2004. https://doi.org/10.1364/bio.2004.sf4.
[40] Jonasson H, Fredriksson I, Bergstrand S, Östgren CJ, Larsson M, Strömberg T. In vivo characterization of light scattering properties of human skin in the 475- to 850-nm wavelength range in a swedish cohort. J Biomed Opt 2018;23(12):1. https://doi.org/10.1117/1.jbo.23.12.121608.
[41] Tearney GJ, Brezinski ME, Southern JF, Bouma BE, Hee MR, Fujimoto JG. Determination of the refractive index of highly scattering human tissue by optical coherence tomography. Opt Lett 1995;20(21):2258–60. https://doi.org/10.1364/OL.20.002258. http://ol.osa.org/abstract.cfm?URI=ol-20-21-2258.
[42] Akarçay HG, Rička J. Simulating light propagation: Towards realistic tissue models. In: Diffuse Optical Imaging III, Optical Society of America, 2011, p. 80880K. https://doi.org/10.1364/ECBO.2011.80880K. http://www.osapublishing.org/abstract.cfm?URI=ECBO-2011-80880K.
[43] Akarçay HG, Hohmann A, Kienle A, Frenz M, Rička J. Monte carlo modeling of polarized light propagation: Stokes vs. Jones. Part II. Appl Opt 2014;53(31):7586–602. https://doi.org/10.1364/AO.53.007586. URL http://ao.osa.org/abstract.cfm?URI=ao-53-31-7586.
[44] Hornung M, Jain A, Frenz M, Akarçay HG. Interpretation of backscattering polarimetric images recorded from multiply scattering systems: a study on colloidal suspensions. Opt Express 2019;27(5):6210–39. https://doi.org/10.1364/OE.27.006210. URL http://www.opticsexpress.org/abstract.cfm?URI=oe-27-5-6210.
[45] Chen AI, Balter ML, Chen MI, Gross D, Alam SK, Maguire TJ, et al. Multilayered tissue mimicking skin and vessel phantoms with tunable mechanical, optical, and acoustic properties, Medical Phys. 2016;43(6Part1): 3117–31. https://doi.org/10.1118/1.4951729.
[46] Lee Y, Hwang K. Skin thickness of korean adults. Surg Radiol Anat 2002;24(3–4):183–9. https://doi.org/10.1007/s00276-002-0034-5.
[47] Ha RY, Nojima K, Adams WP, Brown SA. Analysis of facial skin thickness: Defining the relative thickness index. Plast Reconstr Surg 2005;115(6):1769–73. https://doi.org/10.1097/01.prs.0000161682.63535.9b.
[48] ASTM-International, ASTM G173-03(2012), standard tables for reference solar spectral irradiances: Direct normal and hemispherical on 37 tilted surface, 2012. https://doi.org/10.1520/g0173-03r12. URL www.astm.org.
[49] Wang L-X, Zhou Z-Q, Zhang T-N, Chen X, Lu M. High fill factors of si solar cells achieved by using an inverse connection between MOS and PN junctions. Nanoscale Res Lett 2016;11(1). https://doi.org/10.1186/s11671-016-1678-0.
[50] Alam MK, Khan F, Imtiaz AM. Optimization of subcell interconnection for multi-junction solar cells using switching power converters. IEEE Trans Sustain Energy 2013;4(2):340–9. https://doi.org/10.1109/tste.2012.2223493.
[51] Peraca NM, Bilir DT, Hamadani BH. Frequency response of the external quantum efficiency in multijunction solar cells. Opt Express 2017;25(16):A709. https://doi.org/10.1364/oe.25.00a709.
[52] Nozik A. Quantum dot solar cells. Physica E 2002;14(1–2):115–20. https://doi.org/10.1016/s1386-9477(02)00374-0.
[53] Ranamukhaarachchi SA, Lehnert S, Ranamukhaarachchi SL, Sprenger L, Schneider T, Mansoor I, et al. A micromechanical comparison of human and porcine skin before and after preservation by freezing for medical device development. Sci Rep 2016;6(1). https://doi.org/10.1038/srep32074.
[54] Xue M, Jackson CJ. Extracellular matrix reorganization during wound healing and its impact on abnormal scarring. Adv Wound Care 2015;4(3):119–36. https://doi.org/10.1089/wound.2013.0485.
[55] Sekar SKV, Bargigia I, Mora AD, Taroni P, Ruggeri A, Tosi A, et al. Diffuse optical characterization of collagen absorption from 500 to 1700 nm. J Biomed Opt 2017;22(1):015006https://doi.org/10.1117/1.jbo.22.1.015006.
[56] Grandi G, Ienina A, Bardhi M. Effective low-cost hybrid LED-halogen solar simulator. IEEE Trans Ind Appl 2014;50(5):3055–64. https://doi.org/10.1109/tia.2014.2330003.